



HAL
open science

Contrast-enhanced to non-contrast-enhanced image translation to exploit a clinical data warehouse of T1-weighted brain MRI

Simona Bottani, Elina Thibeau-Sutre, Aurélien Maire, Sebastian Ströer, Didier Dormont, Olivier Colliot, Ninon Burgos

► To cite this version:

Simona Bottani, Elina Thibeau-Sutre, Aurélien Maire, Sebastian Ströer, Didier Dormont, et al.. Contrast-enhanced to non-contrast-enhanced image translation to exploit a clinical data warehouse of T1-weighted brain MRI. BMC Medical Imaging, 2024, 24 (1), pp.67. 10.1186/s12880-024-01242-3 . hal-03497645v2

HAL Id: hal-03497645

<https://hal.science/hal-03497645v2>

Submitted on 21 Mar 2024

HAL is a multi-disciplinary open access archive for the deposit and dissemination of scientific research documents, whether they are published or not. The documents may come from teaching and research institutions in France or abroad, or from public or private research centers.

L'archive ouverte pluridisciplinaire **HAL**, est destinée au dépôt et à la diffusion de documents scientifiques de niveau recherche, publiés ou non, émanant des établissements d'enseignement et de recherche français ou étrangers, des laboratoires publics ou privés.



Distributed under a Creative Commons Attribution 4.0 International License

RESEARCH

Open Access



Contrast-enhanced to non-contrast-enhanced image translation to exploit a clinical data warehouse of T1-weighted brain MRI

Simona Bottani¹, Elina Thibeau-Sutre¹, Aurélien Maire², Sebastian Ströer³, Didier Dormont⁴, Olivier Colliot¹, Ninon Burgos^{1*} and APPRIMAGE Study Group

Abstract

Background Clinical data warehouses provide access to massive amounts of medical images, but these images are often heterogeneous. They can for instance include images acquired both with or without the injection of a gadolinium-based contrast agent. Harmonizing such data sets is thus fundamental to guarantee unbiased results, for example when performing differential diagnosis. Furthermore, classical neuroimaging software tools for feature extraction are typically applied only to images without gadolinium. The objective of this work is to evaluate how image translation can be useful to exploit a highly heterogeneous data set containing both contrast-enhanced and non-contrast-enhanced images from a clinical data warehouse.

Methods We propose and compare different 3D U-Net and conditional GAN models to convert contrast-enhanced T1-weighted (T1ce) into non-contrast-enhanced (T1nce) brain MRI. These models were trained using 230 image pairs and tested on 77 image pairs from the clinical data warehouse of the Greater Paris area.

Results Validation using standard image similarity measures demonstrated that the similarity between real and synthetic T1nce images was higher than between real T1nce and T1ce images for all the models compared. The best performing models were further validated on a segmentation task. We showed that tissue volumes extracted from synthetic T1nce images were closer to those of real T1nce images than volumes extracted from T1ce images.

Conclusion We showed that deep learning models initially developed with research quality data could synthesize T1nce from T1ce images of clinical quality and that reliable features could be extracted from the synthetic images, thus demonstrating the ability of such methods to help exploit a data set coming from a clinical data warehouse.

Keywords Brain MRI, Clinical data warehouse, Image translation

*Correspondence:

Ninon Burgos

ninon.burgos@cncrs.fr

Full list of author information is available at the end of the article



© The Author(s) 2024. **Open Access** This article is licensed under a Creative Commons Attribution 4.0 International License, which permits use, sharing, adaptation, distribution and reproduction in any medium or format, as long as you give appropriate credit to the original author(s) and the source, provide a link to the Creative Commons licence, and indicate if changes were made. The images or other third party material in this article are included in the article's Creative Commons licence, unless indicated otherwise in a credit line to the material. If material is not included in the article's Creative Commons licence and your intended use is not permitted by statutory regulation or exceeds the permitted use, you will need to obtain permission directly from the copyright holder. To view a copy of this licence, visit <http://creativecommons.org/licenses/by/4.0/>. The Creative Commons Public Domain Dedication waiver (<http://creativecommons.org/publicdomain/zero/1.0/>) applies to the data made available in this article, unless otherwise stated in a credit line to the data.

Background

Clinical data warehouses, gathering hundreds of thousands of medical images from numerous hospitals, offer unprecedented opportunities for research. They can for example be used to develop and validate machine learning and deep learning algorithms for the computer-aided diagnosis of neurological diseases. However, they also pose important challenges, a major challenge being their heterogeneity. Neurological diseases can result in a variety of brain lesions that are each studied with specific magnetic resonance imaging (MRI) sequences. For example, T1-weighted (T1w) brain MR images enhanced with a gadolinium-based contrast agent are used to study lesions such as tumors, and T1w images without gadolinium are used to study neurodegenerative diseases.

Computer-aided diagnosis (CAD) systems for neurodegenerative diseases are more and more common in the clinic: they mainly include volumetric analysis, which can be used for the quantitative evaluation of brain atrophy [1–5]. Machine learning systems have been developed for research purposes, but their promising results for the differential diagnosis of neurodegenerative diseases indicate their potential application in the clinic [2, 6, 7]. These CAD systems, both based on volumetric analysis or on machine learning models, rely on features extracted from imaging data. Consequently, CAD systems are reliable only if input features are reliable. Additionally, features extracted from images must be homogeneous no matter the disease, otherwise a link could be established between MRI sequence and pathology, which would create bias. This is critical particularly in a clinical setting as differential diagnosis can be more challenging than in a research setting, as different diseases may co-exist.

Software tools such as SPM [8], ANTs [9] or FSL [10] have been widely used for feature extraction but they were largely validated using structural T1w MRI without gadolinium, to the best of our knowledge, and their good performance on images with gadolinium is thus not guaranteed. We are referring in particular to brain tissue segmentation algorithms: Unified Segmentation for SPM [11], FMRIB's Automated Segmentation Tool (FAST) for FSL [12], and Atropos Multivar-EM Segmentation [13] and Multi-atlas methods [14] for ANTs. A solution could then be to convert contrast-enhanced T1w (T1ce) into non-contrast-enhanced T1w (T1nce) brain MRI before using such tools.

Deep learning has been widely used in the image translation domain. The goal of image translation is to learn a mapping between images of a source modality and images of a target modality, in order to convert an input image of the source modality into an image of the target modality. The U-Net and conditional generative adversarial networks (GANs) appear as the two most popular

options. The U-Net was originally proposed for image segmentation [15, 16]: an encoder with convolutional and downsampling blocks is followed by a decoder with upsampling and convolutional layers. The skip connections linking the encoder and decoder blocks at the same level enable the reconstruction of fine-grained details, explaining the popularity of this architecture for image translation [17–24]. Conditional GANs consist of a generator, which may adopt the U-Net architecture, followed by a discriminator in charge of distinguishing synthetic from real images and challenging the generator so that it improves the quality of the generated images. The good results obtained with conditional GANs explain their wide use for image translation [25–34].

Both U-Net like models and conditional GANs have been proposed for diverse applications. Some aim to enhance the quality of the input images, for example by reducing noise in MRI [35–37] or positron emission tomography [38] images, or by performing super-resolution [25, 27, 39–41]. Other works aim to translate an image of a particular modality into another modality, such as an MRI into an X-ray computed tomography (CT) [19, 20, 24, 29, 17, 30] or a particular MRI sequence into another sequence [31–34]. The U-Net architecture has also been used for data harmonization, e.g. DeepHarmony aims to homogenize the contrast between images coming from different sites [42].

Closer to our application, various deep learning models have been developed for the synthesis of images with gadolinium from images without gadolinium: they include reinforcement learning for liver MRI [43], or Gaussian mixture modeling for CT images [44]. As for the other image translation tasks, 3D U-Net like models have also been used to convert T1nce into T1ce images [45–47]. In two studies [45, 46], multimodal MRI sequences were used as input of the 3D U-Net that was trained and tested on patients with brain cancers. More specifically, the 3D U-Net proposed in [46] predicts patches of T1ce, while the one in [45] directly predicts the full 3D T1ce image. The residual attention U-Net described in [47] outputs synthetic T1nce that are used for the evaluation of cerebral blood volume in mice, instead of the real T1ce.

Our objective in this work was to evaluate how image translation models initially developed using research quality images could be used to exploit a highly heterogeneous data set from a clinical data warehouse by converting T1ce into T1nce images. We thus developed and compared different deep learning models that rely on typical architectures used in the medical image translation domain to convert T1ce into T1nce images. In particular, we implemented 3D U-Net like models with the addition of residual connections, attention modules or transformer layers. We also used these 3D U-Net like

models in a conditional GAN setting. We trained and tested our models using 307 pairs of T1nce and T1ce images coming from a very large clinical data warehouse (39 different hospitals of the Greater Paris area). We first assessed synthesis accuracy by comparing real and synthetic T1nce images using standard metrics. We tested our models both on images of good or medium quality and on images of bad quality to ensure that deep learning models could generate accurate T1nce images no matter the quality of the input T1ce images. We then compared the volumes of gray matter, white matter and cerebrospinal fluid obtained by segmenting the real T1nce, real T1ce and synthetic T1nce images using SPM [11] in order to verify that features extracted from synthetic T1nce were reliable. Preliminary work was accepted for publication in the proceedings of the SPIE Medical Imaging 2022 conference [48]. Contributions specific to this paper include the development of additional models (a 3D U-Net like model with the addition of transformer layers, and three conditional GAN models using different 3D U-Net like models as generators and a patch-based discriminator) and an extended validation of the segmentation task with a deeper analysis of the tissue volume differences.

Materials and methods

Data set description

This work relies on a clinical data warehouse gathering all the T1w brain MR images of adult patients scanned in one of the 39 hospitals of the Greater Paris area (Assistance Publique-Hôpitaux de Paris [AP-HP]). The data were made available by the AP-HP data warehouse and the study was approved by the Ethical and Scientific Board of the AP-HP. According to French regulation, consent was waived as these images were acquired as part of the routine clinical care of the patients.

Among all the images of the clinical data warehouse, we selected only those referring to a 3D brain T1w MRI. This was done thanks to the manual selection by a neuro-radiologist of the DICOM header attributes (in particular the acquisition protocol, the series description and the body part) referring to a 3D brain T1w MRI [49].

In a previous work [49], we developed a quality control framework to identify images that are not proper T1w brain MRIs, to identify acquisitions for which gadolinium was injected, and to rate the overall image quality. The quality score assigned to each image is based on a three-level grade given to three different characteristics: contrast, motion and noise. A grade 0 corresponds to good contrast/no motion/no noise, a grade 1 to medium contrast/some motion/some noise and a grade 2 to bad contrast/severe motion/severe noise. If at least one of the characteristics has a grade of 2, the image is labeled with

a low quality score. If at least one of the characteristics has a grade of 1 and no characteristic has a grade of 2, the image is labeled with a medium quality score. If all characteristics have a grade of level 0, the image is labeled as good quality. We manually annotated 5500 images (out of a batch of 9941 images that were available, excluding images with less than 40 DICOM slices) to train and test convolutional neural network (CNN) classifiers. The graphical interface used to manually annotate the images is publicly available (https://github.com/SimonaBottani/Quality_Control_Interface).

The data set used in this work is composed of 307 pairs of 3D T1ce and T1nce images that were extracted from the batch of 9941 images made available by the AP-HP data warehouse. Their resolution ranges from 0.9 to 1.2 mm. We first selected all the images of low, medium and good quality, excluding images that were not proper T1w brain MRI [49], resulting in 7397 images. This selection was based on manual quality control for 5500 images and on automatic quality control for the remaining 4441 images [49]. In the same way, the presence or absence of gadolinium-based contrast agent was manually noted for 5500 images, while it was obtained through the application of a CNN classifier for the remaining 4441 images. We then considered only patients having both a T1ce and a T1nce image at the same session, with a T1nce image of medium or good quality. Finally, to limit heterogeneity in the training data set, we visually checked all the images and excluded 52 image pairs that were potential outliers because of extremely large lesions (i.e., lesions that substantially altered surrounding brain tissues). Among the selected images, 256 image pairs were of medium and good quality, and 51 image pairs had a T1ce of low quality and a T1nce of good or medium quality. In total the data set comprises 614 images: 534 images were acquired at 3 T and 80 at 1.5 T, 556 images were acquired with a Siemens machine (with seven different models) and 58 with a GE Healthcare machine (with five different models). The workflow in Fig. 1 describes the selection of the data set for our work.

Image preprocessing

All the images were organized following the Brain Imaging Data Structure (BIDS) specification [50]. We applied the following pre-processing using the `t1-linear` pipeline of the open-source software platform Clinica [51], which is a wrapper of the ANTs software [9]. Bias field correction was applied using the N4ITK method [52]. An affine registration to MNI space was performed using ANTs [53]. The registered images were further rescaled based on the min and max intensity values, and cropped to remove background resulting in images of size 169×208×179, with 1 mm isotropic voxels [54]. Finally all the

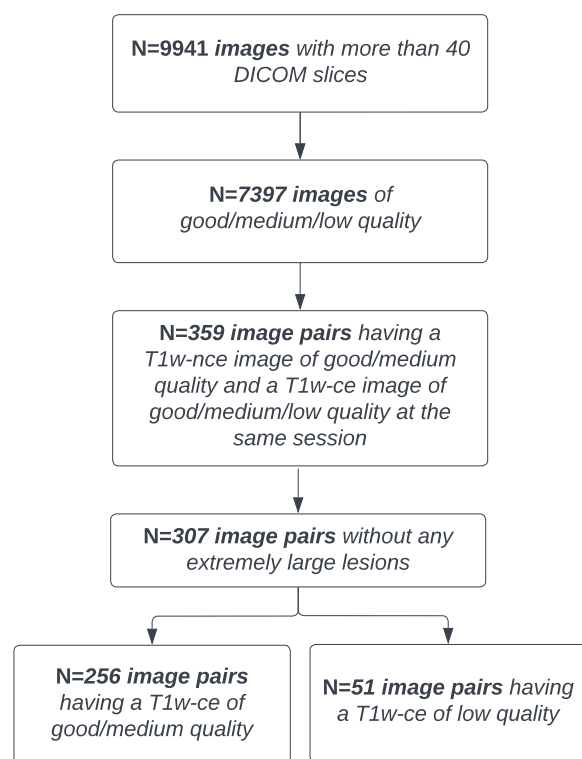


Fig. 1 Description of the different steps for the selection of the data set

images were resampled to have a size of $128 \times 128 \times 128$ using trilinear interpolation in Pytorch.

Network architecture

To generate T1nce from T1ce images, both 3D U-Net like models and conditional GANs were developed and compared. The code used to implement all the architectures and perform the experiments is openly available (https://github.com/SimonaBottani/image_synthesis).

3D U-Net like structures

We implemented three models derived from the 3D U-Net [15, 16]: a 3D U-Net with the addition of residual connections (called *Res-U-Net*) [45, 55], a 3D U-Net with the addition of attention mechanisms (called *Att-U-Net*) [56], and a 3D U-Net with both transformer and convolutional layers (called *Trans-U-Net*) [57] to study how already developed architectures could be adapted to our context, i.e. synthesis from highly heterogeneous images of clinical quality. The U-Net structure allows preserving the details present in the original images thanks to the skip connections [15] and has shown good performance for image-to-image translation [17–24]. Here we detail the three architectures, which are also shown in Fig. 2.

Res-U-Net The *Res-U-Net* we implemented is based on the architecture first proposed by [55] and later used by [45]. The five descending blocks are composed of 3D convolutional layers followed by an instance normalization block and a LeakyReLU (negative slope coefficient $\alpha = 0.2$). The four ascending blocks are composed of transposed convolutional layers followed by a ReLU. The final layer is composed of an upsample module (factor of 2), a 3D convolutional block and a hyperbolic tangent module. Each descending or ascending block is followed by a residual module, which can vary from one to three blocks composed of a 3D convolutional layer and a LeakyReLU ($\alpha = 0.2$). Residual blocks were introduced to avoid the problem of the vanishing gradients in the training of deep neural networks [58]: they ease the training since they improve the flow of the information within the network.

Att-U-Net We implemented the *Att-U-Net* relying on the work of [56]. In this architecture, the five descending blocks are composed of two blocks with a 3D convolutional layer followed by a batch normalization layer and a ReLU. They are followed by four ascending blocks. Each ascending block is composed of an upsample module (factor of 2), a 3D convolutional layer followed by a ReLU, an attention gate and two 3D convolutional layers followed by a ReLU. The attention gate is composed of two 3D convolutional layers, a ReLU, a convolutional layer and a sigmoid layer. Its objective is to identify only salient image regions: the input of the attention gate is multiplied (element-wise multiplication) by a factor (in the range 0–1) resulting from the training of all the blocks of the networks. In this way it discards parts of the images that are not relevant to the task at hand.

Trans-U-Net The *Trans-U-Net* was implemented by [57] (who called the model *TransBTS*). They proposed a 3D U-Net like structure composed of both a CNN and a transformer. The CNN is used to produce an embedding of the input images in order not to lose local information across depth and space. The features extracted by the CNN are the input of the transformer whose aim is to model the global features. The descending blocks are composed of four different blocks, each being composed of a 3D convolutional layer and one, two or three blocks composed of a batch normalization layer, a ReLU and another 3D convolutional layer. The model is then composed of four transformer layers, after a linear projection of the features. Each transformer layer is itself composed of a multi-head attention block and a feed forward network. The four ascending blocks are composed of a 3D convolutional layer and one or two blocks with a batch normalization layer, a ReLU, a 3D convolutional layer followed by a 3D deconvolutional layer. The

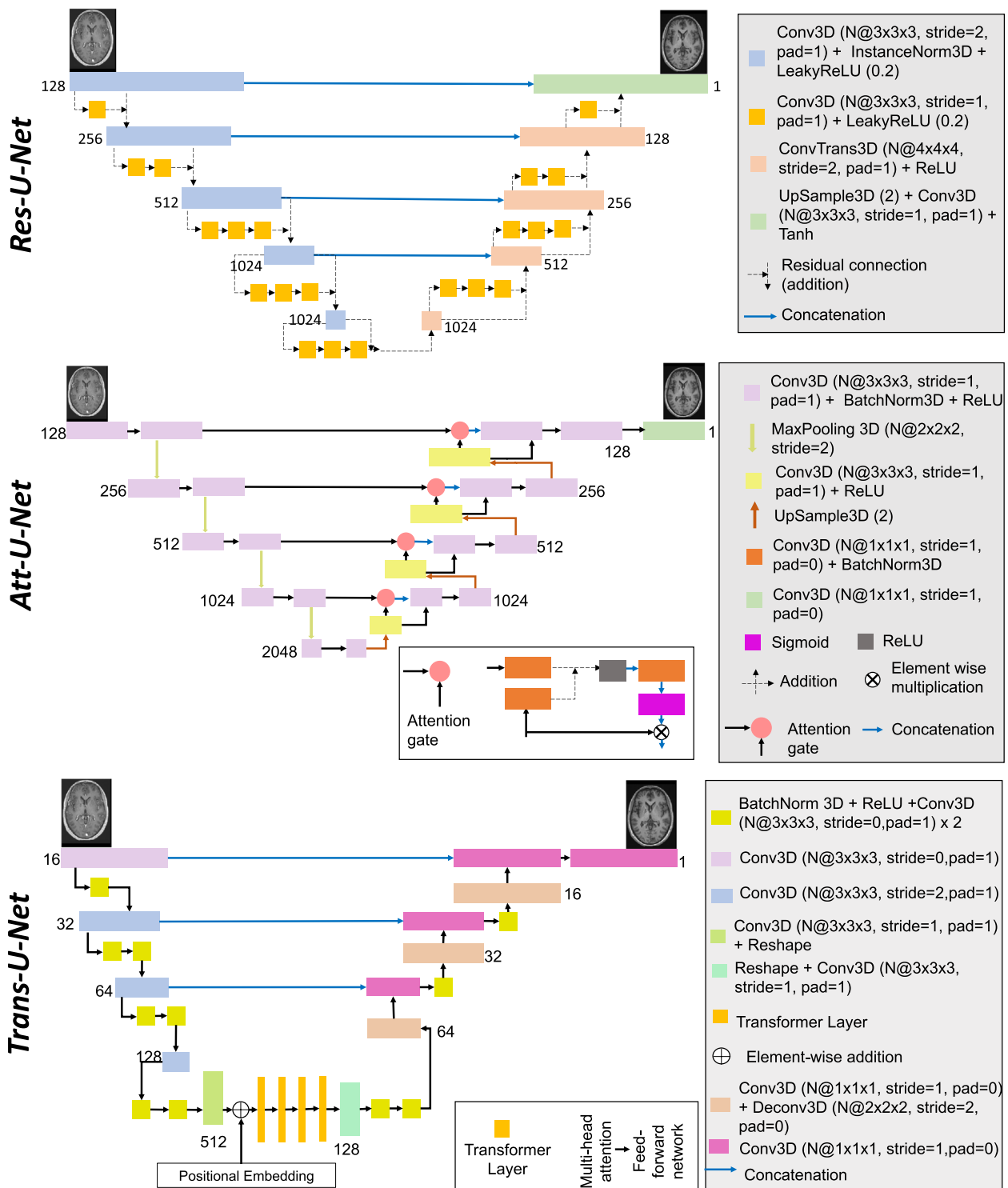


Fig. 2 Architectures of the proposed 3D U-Net like models. The models take as input a real T1nce image of size 128x128x128 and generate a synthetic T1nce of size 128x128x128. *Res-U-Net*: images pass through five descending blocks, each one followed by a residual module, and then through four ascending blocks and one final layer. *Att-U-Net*: images pass through five descending blocks and then through four ascending blocks and one final layer. One of the inputs of each ascending block is the result of the attention gate. *Trans-U-Net*: images pass through four descending blocks, four transformer layers and four ascending layers. All the parameters such as kernel size, stride, padding, size of each feature map (N) are reported

final layer is composed of a 3D convolutional layer and a soft-max layer.

For the three 3D U-Net like models we used the same training parameters. We used the Adam optimizer, the L_1 loss, a batch size of 2 and trained during 300 epochs. The model with the best loss, determined using the training set, was saved as final model. We relied on Pytorch for the implementation.

Conditional GANs

Generative adversarial networks (GANs) were first introduced by [59]. They are generative deep learning models composed of two elements: a generator for synthesizing new examples and a discriminator for classifying whether examples are real, i.e. the original ones, or fake, i.e. synthesized by the generator. Conditional GANs (cGANs) [60] are a variant of GANs where the generator and the discriminator are conditioned by the true samples. They can only be used with paired data sets.

We propose three different cGAN models that differ in the architecture of the generators, which correspond to the three architectures presented above. The discriminator is the same for all the cGANs: it is a 3D patch CNN, first proposed by [61] and used in the medical image translation domain [62, 63]. Its aim is to classify if each pair of patches contains two real images, or a real and a fake image. The advantages of working with patches is that the discriminator focuses on the details of the images and the generator must improve them to fool the discriminator.

Our discriminator is made of four blocks: the first three blocks are composed of a 3D convolutional layer followed by a LeakyReLU (negative slope coefficient $\alpha = 0.2$), and the last block is composed of a 3D convolutional layer and a 3D average pooling layer. From images of size $128 \times 128 \times 128$, we created eight patches of size $64 \times 64 \times 64$ with a stride of 50.

For the training of the discriminator we used the least square loss as proposed in [64] in order to increase the stability, thus avoiding the problem of vanishing gradients that occurs with the usual cross-entropy loss. Stability of the training was also improved using soft labels: random numbers between 0 and 0.3 represented real images and random numbers between 0.7 and 1 represented fake images.

The total loss of the cGANs combines

- the loss of the generator composed of the sum of the L_1 loss (i.e. pixel-wise absolute error) computed between the generated and true images, and the least square loss computed between the predicted probabilities of the generated images and positive labels

$$L_G = -\log [p(\text{synthetic T1nce})] + L_1(\text{T1nce}, \text{synthetic T1nce}) \quad (1)$$

with $p(X)$ the probability returned by the discriminator that the image X is real.

- the loss of the discriminator composed of the mean of the least square loss computed between the predicted probabilities of the true images and positive labels, and the least square loss computed between the predicted probabilities of the generated images and negative labels

$$L_D = -0.5 \log [p(\text{T1nce})] - 0.5 \log [1 - p(\text{synthetic T1nce})]. \quad (2)$$

At first, both the generators and discriminators were pre-trained separately. The adversarial nature of GANs makes their training time consuming. In our experimental setting, constrained by the computational resources available within the clinical data warehouse, we have found out that using a pretrained generator and discriminator, each with an already established good performance, can stabilize the training of the cGAN. In particular, we have seen that it can prevent the vanishing gradient effect in the discriminator. This was observed experimentally, but other works have described the advantages of pretrained models [65–67]. Regarding each generator, we reused the best model obtained previously. The discriminators were pretrained for the recognition of real and fake patches (fake images were obtained from each pretrained generator). The generators and discriminators were then trained together. The generator models with the best loss, determined using the training set, were saved as final models. Note that the batch size was set to 1 due to limited computing resources.

Experiments and validation measures

The experiments relied on 307 pairs of T1ce and T1nce images. We randomly selected 10% of the 256 image pairs of medium and good quality for testing (data set called $\text{Test}_{\text{good}}$), the other 230 image pairs being used for training. Only images of good and medium quality were used for training to ensure that the model focuses on the differences related to the presence or absence of gadolinium, and not to other factors. The remaining 51 image pairs with a T1ce of low quality and a T1nce of good or medium quality were used only for testing (data set called Test_{low}).

Synthesis accuracy

Image similarity was evaluated using the mean absolute error (MAE), peak signal-to-noise ratio (PSNR) and structural similarity (SSIM) [68]. The MAE is the mean of each absolute value of the difference between the true pixel and the generated pixel and PSNR is a function of the mean squared error: these two metrics allow

a direct comparison between the synthetic image and the real one. The SSIM aims to measure quality by capturing the similarity of images, it is a weighted combination of the luminance, contrast and structure. For the MAE, the minimum value is 0 (the lower, the better), for PSNR the maximum value is infinite (the higher, the better) and for SSIM the maximum value is 1 (the higher, the better). We calculated these metrics both between the real and synthetic T1nce images and between the real T1nce and T1ce images (as reference). These metrics were calculated within the brain as this region is the main focus of our evaluation. A brain mask was obtained for each subject by skull-stripping the T1nce and T1ce images using HD-BET [69] and computing the union of the two resulting brain masks.

Segmentation fidelity

Our goal is to obtain gray matter (GM), white matter (WM) and cerebrospinal fluid (CSF) segmentations from T1ce images using widely-used software tools that are consistent with segmentations obtained from T1nce images. We thus assessed segmentation consistency by analyzing the tissue volumes resulting from the segmentations, which are important features when studying atrophy in the context of neurodegenerative diseases. We used the algorithm proposed in SPM [11] but these features can be obtained with commercial tools, such as NeuroreaderTM, volBrain, NeuroQuant or Inbrain, and used in a clinical setting [1–6].

The volumes of the different tissues were obtained as follows. At first, synthetic T1nce images were resampled back to a size of $169 \times 208 \times 179$ using trilinear interpolation in Pytorch so that real and synthetic images have the same grid size. We processed the images using the `t1-volume-tissue-segmentation` pipeline of Clinica [51, 70]. This wrapper of the Unified Segmentation procedure implemented in SPM [11] simultaneously performs tissue segmentation, bias correction and spatial normalization. Once the probability maps were obtained for each tissue, we computed the maximum probability to generate binary masks and we multiplied the number of voxels by the voxel dimension to obtain the volume of each tissue. We calculated both the absolute volume difference (AVD) and the volume difference (VD) for each tissue between the real T1ce or synthetic T1nce and the real T1nce as follows:

$$AVD = \frac{|V_t^I - V_t^J|}{TIV^I} \times TIV, \quad (3a)$$

$$VD = \frac{V_t^I - V_t^J}{TIV^I} \times TIV, \quad (3b)$$

where V_t^I is the volume of tissue t extracted from the real T1nce image I , V_t^J is the volume of tissue t extracted from

image J , J being the synthetic T1nce or real T1ce image. TIV^I corresponds to the total intracranial volume (sum of the gray matter, white matter and cerebrospinal fluid volumes) obtained from the real T1nce image I and TIV corresponds to the average total intracranial volume computed across the two test sets. The multiplication by the average total intracranial volume (TIV) aims at obtaining volumes (in cm^3) rather than fractions of the TIV of each subject, which is easier to interpret. Since this is a multiplication by a constant, it has no impact on the results. To assess whether the tissue volumes presented a statistically significant difference in terms of AVD depending on the images they were obtained from, we performed paired t-tests using Bonferroni correction for multiple comparisons.

In addition, we compared the binary tissue maps extracted from the real T1ce or synthetic T1nce image to those extracted from the real T1nce using the Dice score.

Results

We report results for the proposed generator-only 3D U-Net like models and cGANs trained on 230 image pairs of good and medium quality, and tested on $\text{Test}_{\text{good}}$ and Test_{low} obtained from a clinical data set.

Examples of synthetic T1nce images obtained with the *cGAN Att-U-Net* model together with the real T1ce and T1nce images are displayed in Fig. 3. Images of patients A and B belong to $\text{Test}_{\text{good}}$ while images of patients C and D belong to Test_{low} . We note the absence of contrast agent in the synthetic T1nce, while it is clearly visible in the sagittal slice of the T1ce (particularly visible for patients A and C) and that the anatomical structures are preserved between the synthetic and real T1nce, even in the case of a disease (as for patient B). We also note that contrast between gray and white matter is preserved in the synthetic T1nce (particularly visible for patients B and D). For Test_{low} , the contrast seems improved in the synthetic compared with the real T1ce image (especially for patient D). This results is not surprising as the networks were trained with images of medium or good quality, which will have on average a better contrast than images of low quality.

Synthesis accuracy

Table 1 reports the image similarity metrics obtained for the two test sets within the brain region. We computed these metrics to assess the similarity between real and synthetic T1nce images, but also between T1nce and T1ce images to set a baseline. We observe that, for all models, the similarity is higher between real and synthetic T1nce images than between T1nce and T1ce images according to all three metrics on both test sets. The differences observed in terms of MAE, PSNR and

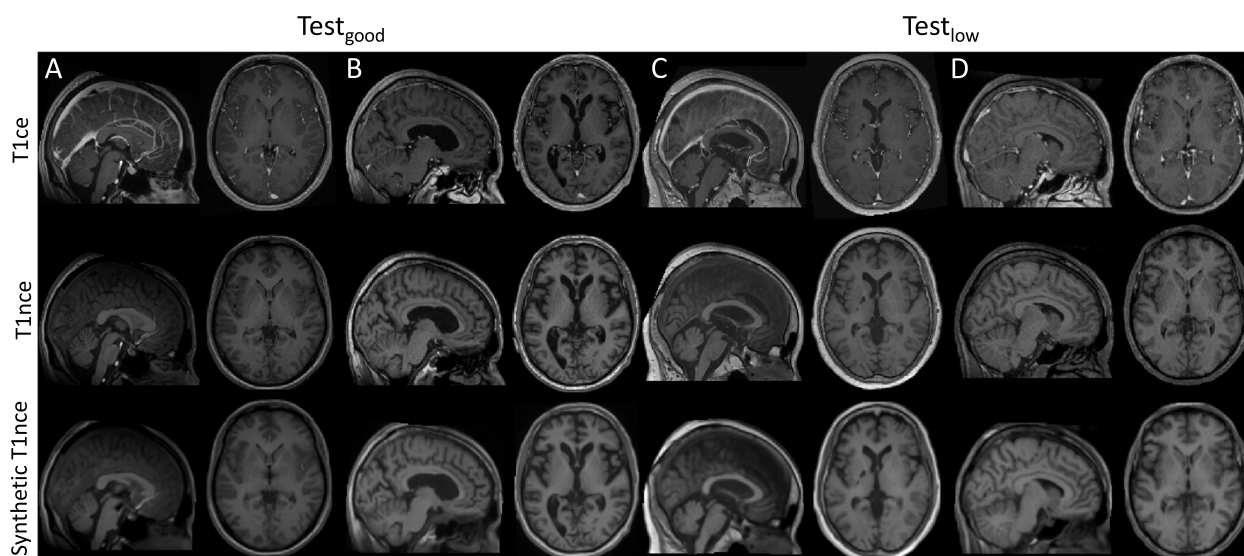


Fig. 3 Examples of real T1ce (top), real T1nce (middle) and synthetic T1nce obtained with the *cGAN Att-U-Net* model (bottom) images in the sagittal and axial planes. Images of patients A and B belong to $\text{Test}_{\text{good}}$ (left) while images of patients C and D belong to Test_{low} (right)

Table 1 MAE, PSNR and SSIM obtained on the two independent test sets with various image quality. For each metric, we report the average and standard deviation across the corresponding test set. We compute the metrics for both real T1ce and synthetic T1nce in relation to the real T1nce, and so within the brain region

Test set	Compared images	Model	MAE (%)	PSNR (dB)	SSIM
$\text{Test}_{\text{good}}$	T1nce / T1ce	-	4.14 ± 1.59	23.03 ± 2.83	0.90 ± 0.05
	T1nce / Synthetic T1nce	<i>Res-U-Net</i>	3.06 ± 1.50	26.89 ± 4.30	0.95 ± 0.04
		<i>Att-U-Net</i>	2.73 ± 1.69	29.07 ± 4.53	0.96 ± 0.05
		<i>Trans-U-Net</i>	2.80 ± 1.42	28.00 ± 4.13	0.96 ± 0.04
		<i>cGAN Res-U-Net</i>	3.47 ± 1.59	23.89 ± 4.30	0.95 ± 0.04
		<i>cGAN Att-U-Net</i>	2.69 ± 1.68	28.89 ± 4.44	0.97 ± 0.05
		<i>cGAN Trans-U-Net</i>	2.86 ± 1.59	28.00 ± 4.32	0.96 ± 0.04
Test_{low}	T1nce / T1ce	-	3.71 ± 1.99	24.20 ± 3.85	0.91 ± 0.06
	T1nce / Synthetic T1nce	<i>Res-U-Net</i>	2.93 ± 1.77	26.71 ± 4.32	0.95 ± 0.05
		<i>Att-U-Net</i>	2.89 ± 1.85	27.15 ± 4.57	0.95 ± 0.05
		<i>Trans-U-Net</i>	2.98 ± 1.89	26.71 ± 4.38	0.94 ± 0.05
		<i>cGAN Res-U-Net</i>	3.20 ± 1.96	26.20 ± 4.42	0.93 ± 0.05
		<i>cGAN Att-U-Net</i>	2.86 ± 1.83	27.12 ± 4.50	0.95 ± 0.05
		<i>cGAN Trans-U-Net</i>	2.97 ± 1.83	26.68 ± 4.40	0.94 ± 0.05

SSIM between the baseline and each image translation approach are statistically significant (corrected p -value < 0.05 according to a paired t-test corrected for multiple comparisons using the Bonferroni correction).

Among the generator-only 3D U-Net like models, the *Att-U-Net* performed slightly better than the others, both for $\text{Test}_{\text{good}}$ (mean MAE: 2.73%, PSNR: 29.07 dB, SSIM: 0.96) and Test_{low} (mean MAE: 2.89%, PSNR: 27.18 dB, SSIM: 0.95). The performance of the cGANs were comparable to

their counterparts composed only of the generator. *cGAN Att-U-Net* had a lower MAE for both test sets (mean MAE: 2.69% for $\text{Test}_{\text{good}}$ and mean MAE: 2.86% for Test_{low}). There was no statistically significant difference observed, no matter the synthesis accuracy measure, between *cGAN Att-U-Net*, the best performing model according to the MAE, and the other approaches for both test sets (corrected p -value > 0.05). For further validation we kept only the generator-only *Att-U-Net* and *cGAN Att-U-Net*.

Segmentation fidelity

Examples of probability gray matter maps obtained from T1ce, T1nce and synthetic T1nce images are displayed in Fig. 4. Compared with the T1ce images, the gray matter maps obtained from the synthetic T1nce better resembles that extracted from the T1nce, especially for Test_{low} .

Absolute volume differences (AVD) obtained between T1nce and T1ce images and between T1nce and synthetic T1nce images (obtained with the generator-only *Att-U-Net* model and the *cGAN Att-U-Net*) for GM, WM and CSF are reported in Table 2. For both test sets and all tissues, the absolute volume differences are smaller between T1nce and synthetic T1nce images than between T1nce and T1ce images for the two models. Using the generator-only *Att-U-Net* on $\text{Test}_{\text{good}}$, absolute volume differences of GM and CSF between T1nce/T1ce and T1nce/Synthetic T1nce are statistically significantly different (corrected p -value < 0.01 according to a paired t-test corrected for multiple comparisons using the Bonferroni correction), while on Test_{low} absolute volume differences of all the tissues are statistically significantly different (corrected p -value < 0.01). Using the *cGAN Att-U-Net* model, absolute volume differences of all the tissues are statistically significantly different (corrected p -value < 0.01) for both test sets. This means that there is an advantage in using synthetic T1nce images rather than T1ce images, no

matter the model used for the synthesis: segmentation of GM, CSF and WM is more reliable since closer to the segmentation of the tissues in the real T1nce.

Volume differences (VD) computed between T1nce and T1ce images and between T1nce and synthetic T1nce images (obtained with the generator-only *Att-U-Net* and *cGAN Att-U-Net*) for GM, WM and CSF are reported in Fig. 5. We observe that volumes extracted from T1ce images tend to be over-estimated (GM) or under-estimated (CSF) and that most of these biases disappear when tissues are extracted from synthetic T1nce images (mean VD closer to 0).

The Dice scores obtained when comparing the GM, WM and CSF segmentations between T1nce and T1ce images and between T1nce and synthetic T1nce images (obtained with the generator-only *Att-U-Net* and the *cGAN Att-U-Net*) are displayed in Table 3. We observe that for both gray and white matter, the Dice scores are similar between T1nce and T1ce or synthetic T1nce images, while for CSF higher Dice scores are obtained using synthetic T1nce images.

Discussion

The use of clinical images for the validation of computer-aided diagnosis systems is still largely unexplored. One of the obstacles lies in the heterogeneity of the data acquired in the context of routine clinical practice.

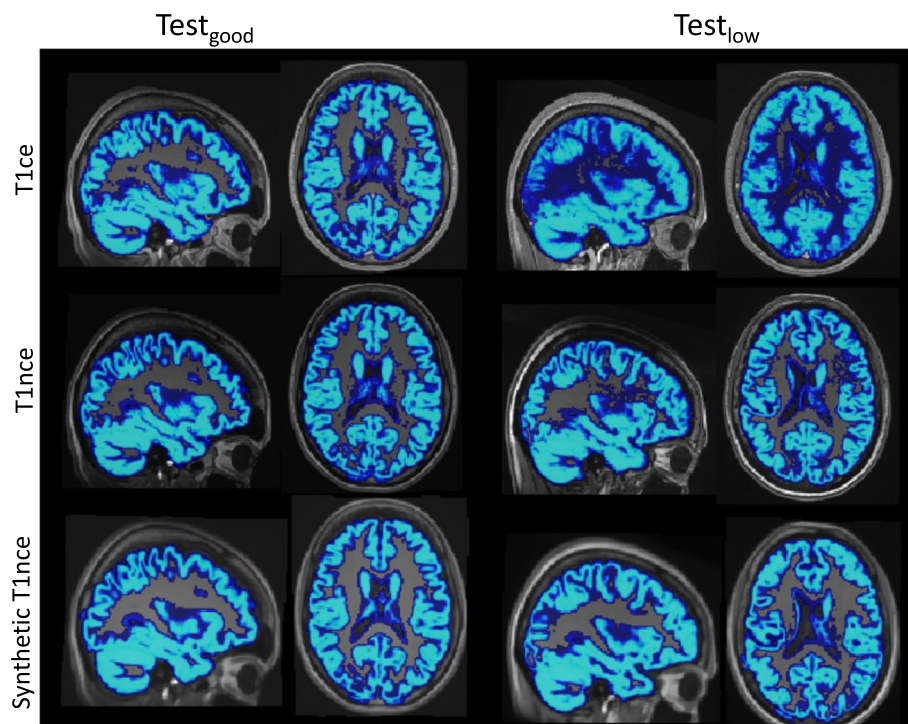


Fig. 4 Example of the probability gray matter maps obtained from T1ce (top), T1nce (middle) and synthetic T1nce (*cGAN Att-U-Net* model, bottom) images from $\text{Test}_{\text{good}}$ (left) and Test_{low} (right)

Table 2 Absolute volume difference (mean ± standard deviation in cm³) between T1nce and T1ce images and between T1nce and synthetic T1nce images (obtained with the generator-only *Att-U-Net* and *cGAN Att-U-Net* models) for gray matter, white matter and cerebrospinal fluid (CSF). * indicates that the absolute volume difference between T1nce and synthetic T1nce images is statistically significantly different from that of the baseline (corrected *p*-value <0.01) according to a paired t-test corrected for multiple comparisons using the Bonferroni correction

	Compared images	Model	Test _{good} [cm ³]	Test _{low} [cm ³]
Gray matter	T1nce / T1ce	-	26.68 ± 15.92	49.63 ± 49.38
	T1nce / Synthetic T1nce	<i>Att-U-Net</i>	10.36 ± 6.98 *	19.61 ± 29.54 *
		<i>cGAN Att-U-Net</i>	9.24 ± 6.10 *	19.67 ± 28.32 *
White matter	T1nce / T1ce	-	10.81 ± 3.71	25.36 ± 27.73
	T1nce / Synthetic T1nce	<i>Att-U-Net</i>	7.79 ± 5.87	13.95 ± 24.74 *
		<i>cGAN Att-U-Net</i>	6.40 ± 4.43 *	14.49 ± 21.06 *
CSF	T1nce / T1ce	-	61.62 ± 34.61	69.55 ± 37.77
	T1nce / Synthetic T1nce	<i>Att-U-Net</i>	13.37 ± 10.18 *	12.25 ± 7.72 *
		<i>cGAN Att-U-Net</i>	18.27 ± 17.20 *	17.10 ± 18.45 *

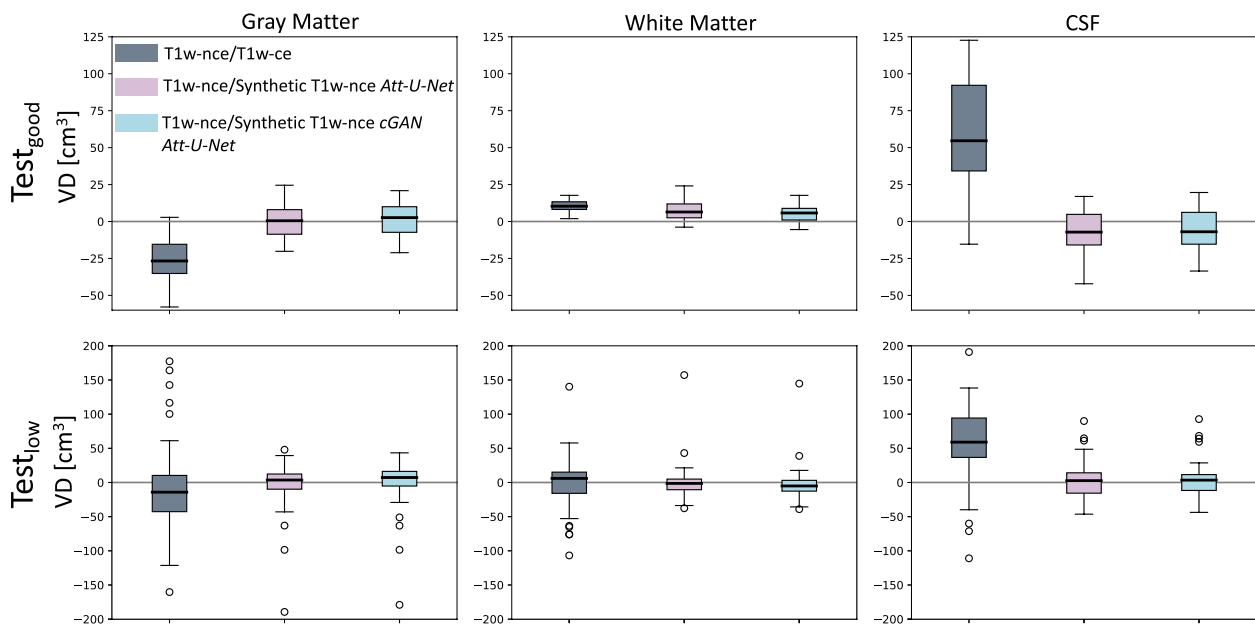


Fig. 5 Volume differences (VD) in cm³ between T1nce and T1ce images and between T1nce and synthetic T1nce images (obtained with the generator-only *Att-U-Net* and the *cGAN Att-U-Net* models) for gray matter (left), white matter (middle) and cerebrospinal fluid (CSF, right) for both Test_{good} (top) and Test_{low} (bottom)

Post-acquisition homogenization is crucial because, contrary to research data, no strict acquisition protocols, that would ensure a certain homogeneity among the images, exist for clinical data. Heterogeneity originates from the fact that images are acquired with different scanners at different field strengths during a large period of time and because patients may suffer from a large variety of diseases. Homogenization of clinical data sets of 3D T1w brain MRI, and consequently of the features extracted from them, is an important step for the development of reliable CAD systems. Indeed, when training

a CAD system, the algorithms must not be affected by the data set variations even though clinical images may greatly vary.

A source of heterogeneity among clinical data sets is the fact that they contain a mix of images acquired with and without gadolinium-based contrast agent. In our case, among the 7397 proper T1w brain images made available by the AP-HP data warehouse out of a batch of 9941 images, 59% of the images were contrast-enhanced [49]. As a first step towards the homogenization of this data set, we thus proposed a framework to convert T1ce

Table 3 Dice scores obtained when comparing the gray matter, white matter and cerebrospinal fluid (CSF) segmentations between T1nce and T1ce images and between T1nce and synthetic T1nce images (obtained with the generator-only *Att-U-Net* and the *cGAN Att-U-Net*)

	Compared images	Model	Test _{good}	Test _{low}
Gray matter	T1nce / T1ce	-	0.88 ± 0.02	0.77 ± 0.12
	T1nce / Synthetic T1nce	<i>Att-U-Net</i> <i>cGAN Att-U-Net</i>	0.87 ± 0.02 0.87 ± 0.02	0.81 ± 0.07 0.81 ± 0.07
White matter	T1nce / T1ce	-	0.93 ± 0.01	0.85 ± 0.10
	T1nce / Synthetic T1nce	<i>Att-U-Net</i> <i>cGAN Att-U-Net</i>	0.90 ± 0.02 0.91 ± 0.02	0.86 ± 0.04 0.86 ± 0.03
CSF	T1nce / T1ce	-	0.63 ± 0.10	0.62 ± 0.10
	T1nce / Synthetic T1nce	<i>Att-U-Net</i> <i>cGAN Att-U-Net</i>	0.80 ± 0.05 0.80 ± 0.05	0.78 ± 0.07 0.78 ± 0.07

images into T1nce images using deep learning models. The choice to synthesize T1nce images from T1ce images was constrained by the fact that software tools for feature extraction in the neuroimaging community were developed for T1nce MRI. To the best of our knowledge, none of these tools has largely been applied to the extraction of features from T1ce MRI data and their performance in this scenario is thus mostly unknown.

The contribution of our work consists in the development and validation of deep learning models (generator-only U-Net models and conditional GANs) for the translation of T1ce to T1nce images coming from a clinical data warehouse. We compared three 3D U-net models differentiated by the addition of residual modules, of attention modules or of transformer layers, used as simple generators and also within a conditional GAN setting with the addition of a patch-based discriminator. These models have widely been used for the image translation of medical images [71, 72], but to the best of our knowledge, their application to clinical data has not been proven yet. The proposed models were trained using 230 image pairs and tested on two different test sets: 26 image pairs had both a T1nce and T1ce of good or medium quality and 51 image pairs had a T1nce of good or medium quality and a T1ce of bad quality. Having two test sets of different qualities is a key point since we are dealing with a real clinical heterogeneous data set (e.g., acquisitions from 12 scanner models), where images of low quality, corresponding in majority to T1ce images with a low contrast, may represent 30% of the data [49].

We first assessed the similarity between real and synthetic T1nce images and between real T1nce and T1ce images using three similarity metrics, MAE, PSNR and SSIM. We showed that the similarity between real and synthetic T1nce images was higher than the similarity between real T1nce and T1ce images according to all the metrics, no matter the models used nor the quality

of the input image. The synthesis accuracy obtained with the models evaluated was of the same order as the one reached in recent works on non-contrast-enhanced to contrast-enhanced image translation [45, 46]. The performance of all the models was equivalent (no statistically significant difference observed), meaning that all were able to synthesize T1nce images. Slightly better performance was reached with the addition of attention modules (generator-only *Att-U-Net* and *cGAN Att-U-Net* models), and these models were thus further evaluated. Note that the image similarity metrics were computed within the brain region, as this was the main focus of our work, and that another conclusion could have been reached when computing these metrics for the whole head.

In the second step of the validation, we assessed the similarity of features extracted from the different images available using a widely adopted segmentation framework known for its robustness, SPM [8, 11]. For the evaluation of the segmentation, we reported the absolute volume difference, the volume difference and the Dice scores. We showed that the absolute volume differences of GM, WM and CSF were larger between real T1nce and T1ce images than between real and synthetic T1nce images (statistically significant difference most of the times, systematically for GM which is the main feature when studying atrophy in neurodegenerative diseases). This confirms the hypothesis that gadolinium-based contrast agent may alter the contrast between the different brain tissues, making features extracted from such images with standard segmentation tools, here SPM [8, 11], unreliable. At the same time, we validated the suitability of the synthetic images since their segmentation was consistent with those obtained from real T1nce images as the absolute volume differences were small. The fact that the differences between the volumes extracted from the real and synthetic T1nce images are relatively close to zero show

that the tissue volumes are not systematically under- or over-estimated when extracted from the synthetic images. When analyzing the Dice scores in the gray matter and white matter, we observed that they are mostly equivalent when computed between real T1nce and T1ce or between real and synthetic T1nce. The improvement brought by the synthetic T1nce is only observed in the CSF. This is slightly different from what was observed when analyzing the absolute volume differences. This is due to the fact that the Dice score is normalized and that we report the volume difference in cm^3 . Nevertheless, we mainly focused on the analysis of the volume differences because the goal of our work is to use volumetric features as input for machine learning or deep learning models for computer-aided diagnosis. Future work could consist in extending the volumetric analysis to subcortical regions. It could also consist in further evaluating our approach on surface-based features such as cortical thickness.

Even though the synthetic T1nce images enable the extraction of reliable features, their quality could still be improved. Many constraints exist when working with data from a clinical data warehouse. One is the fact that these data are accessible only through a closed environment provided by the IT department of the AP-HP as described in [73]. Limitations in computational resources and storage space make training deep learning models difficult, which limits the experiments that can be performed to find the optimal model. In particular, in order to have as much data as possible for training, we decided to split our data set in just a training and two test sets for this work. With more data and more computational resources, a proper split into training, validation and test sets would have been more suitable. The proposed models could be improved by better optimizing the hyperparameters (such as the learning rate or the size of the kernels), adding a perceptual loss when training the conditional GANs [74] or adding more layers in the patch-based discriminator. Other architectures could also be explored. We have restricted our work to conditional GANs, which need paired data to be trained, but we could exploit more data working with cycle GANs [75] as they can deal with unpaired data.

In any case, several steps remain to be performed before using synthetic T1nce images for the differential diagnosis of neurological diseases in a clinical setting. First, the preprocessing steps should be minimized. This would for example imply using images in their native space instead of images spatially normalized to the MNI space as we did in this work to ease the evaluation of the approach. In addition, the performance of CAD systems trained with a mix of real T1nce and T1ce images should be compared with the performance of CAD systems trained with a mix of real and synthetic T1nce images.

To prevent introducing a correlation between image properties (e.g. smoothness) and pathology, which would bias the classification performance, it may be necessary to also feed the real T1nce images to the neural network and use the resulting images as inputs of the CAD system, as suggested in [42]. Furthermore, heterogeneity within a clinical data set can arise from other sources, such as the use of different MRI scanner machines or different acquisition parameters. Future works should study their influence and propose models to achieve a more general homogenization, as proposed in [76]. Thanks to these improvements, the application of the proposed homogenization framework would not be limited to differential diagnosis but could be extended to the study of disease progression, which requires capturing more subtle volume differences.

Conclusions

Clinical data warehouses offer fantastic opportunities for computer-aided diagnosis of neurological diseases but their heterogeneity must be reduced to avoid biases. As a first step to homogenize such a large clinical data set, this work proposed to convert images acquired after the injection of gadolinium into non-contrast-enhanced images using 3D U-Net models and conditional GANs. Validation using standard image similarity measures demonstrated that the similarity between real and synthetic T1nce images was higher than between real T1nce and T1ce images for all the models compared. We also showed that features extracted from the synthetic images (GM, WM and CSF volumes) were closer to those obtained from the T1nce brain MR images (considered as reference) than the original T1ce images. These results demonstrate the ability of deep learning methods to help exploit a data set coming from a clinical data warehouse.

Acknowledgements

The research was done using the Clinical Data Warehouse of the Greater Paris University Hospitals. The authors are grateful to the members of the AP-HP WIND and URC teams, and in particular Stéphane Bréant, Florence Tubach, Jacques Ropers, Antoine Rozès, Camille Nevoret, Christel Daniel, Martin Hilka, Yannick Jacob, Cyrina Saussol, Julien Dubiel, Faerber Philippe, Mmaka Ibrahim and Gozlan Rafel. They would also like to thank the "Collégiale de Radiologie of AP-HP" as well as, more generally, all the radiology departments from AP-HP hospitals.

APPRIMAGE Study Group

Olivier Colliot, Ninon Burgos, Simona Bottani, Sophie Loizillon⁵, Didier Dormont^{5,6}, Stéphane Lehericy^{6,25,26}, Samia Si Smail Belkacem, Sebastian Ströer⁶, Nathalie Boddaert⁷, Farida Benoudiba, Ghaida Nasser, Claire Ancelet, Laurent Spelle⁸, Aurélien Maire, Stéphane Bréant, Christel Daniel, Martin Hilka, Yannick Jacob, Julien Dubiel, Cyrina Saussol, Rafael Gozlan²³, Florence Tubach, Jacques Ropers, Antoine Rozès, Camille Nevoret²⁴, Hubert Ducou-Le-Pointe⁹, Catherine Adamsbaum¹⁰, Marianne Alison¹¹, Emmanuel Houdart¹², Robert Carlier^{13,21}, Myriam Edjlali¹³, Betty Marro^{14,15}, Lionel Arrive¹⁴, Alain Luciani¹⁶, Antoine Khalil¹⁷, Elisabeth Dion¹⁸, Laurence Rocher¹⁹, Pierre-Yves Brillet²⁰, Paul Legmann, Jean-Luc Drape²²

- ⁵Sorbonne Université, Institut du Cerveau - Paris Brain Institute, Inserm, CNRS, AP-HP, Hôpital de la Pitié Salpêtrière, Inria, Aramis project-team, F-75013, Paris, France
- ⁶AP-HP, Hôpital de la Pitié Salpêtrière, Department of Neuroradiology, F-75013, Paris, France
- ⁷AP-HP, Hôpital Necker, Department of Radiology, F-75015, Paris, France
- ⁸AP-HP, Hôpital Bicêtre, Department of Radiology, F-94270, Le Kremlin-Bicêtre, France
- ⁹AP-HP, Hôpital Armand-Trousseau, Department of Radiology, F-75012, Paris, France
- ¹⁰AP-HP, Hôpital Bicêtre, Department of Pediatric Radiology, F-94270, Le Kremlin-Bicêtre, France
- ¹¹AP-HP, Hôpital Robert-Debré, Department of Radiology, F-75019, Paris, France
- ¹²AP-HP, Hôpital Lariboisière, Department of Neuroradiology, F-75010, Paris, France
- ¹³AP-HP, Hôpital Raymond-Poincaré, Department of Radiology, F-92380, Garches, France
- ¹⁴AP-HP, Hôpital Saint-Antoine, Department of Radiology, F-75012, Paris, France
- ¹⁵AP-HP, Hôpital Tenon, Department of Radiology, F-75020, Paris, France
- ¹⁶AP-HP, Hôpital Henri-Mondor, Department of Radiology, F-94000, Créteil, France
- ¹⁷AP-HP, Hôpital Bichat, Department of Radiology, F-75018, Paris, France
- ¹⁸AP-HP, Hôpital Hôtel-Dieu, Department of Radiology, F-75004, Paris, France
- ¹⁹AP-HP, Hôpital Antoine-Béclère, Department of Radiology, F-92140, Clamart, France
- ²⁰AP-HP, Hôpital Avicenne, Department of Radiology, F-93000, Bobigny, France
- ²¹AP-HP, Hôpital Ambroise Paré, Department of Radiology, F-92100 104, Boulogne-Billancourt, France
- ²²AP-HP, Hôpital Cochin, Department of Radiology, F-75014, Paris, France
- ²³AP-HP, Innovation & Données – Département des Services Numériques, F-75012, Paris, France
- ²⁴AP-HP, Unité de Recherche Clinique, Hôpital de la Pitié Salpêtrière, Department of Neuroradiology, F-75013, Paris, France
- ²⁵ICM, Centre de NeuroImagerie de Recherche - CENIR, Paris, France
- ²⁶Sorbonne Université, Institut du Cerveau - Paris Brain Institute, Inserm, CNRS, AP-HP, Hôpital de la Pitié Salpêtrière, F-75013, Paris, France.

Authors' contributions

SB implemented the study, interpreted the data, drafted the manuscript and implemented software. ETS implemented software. AM, ST contributed to the analysis of data. DD, OC and NB designed the study. OC and NB provided funding, participated to the interpretation of the data and substantively revised the manuscript. All authors read and approved the final manuscript.

Funding

The research leading to these results has received funding from the Abeona Foundation (project Brain@Scale), from the French government under management of Agence Nationale de la Recherche as part of the "Investissements d'avenir" program, reference ANR-19-P3IA-0001 (PRAIRIE 3IA Institute) and reference ANR-10-IAIHU-06 (Agence Nationale de la Recherche-10-IA Institut Hospitalo-Universitaire-6). The funding bodies played no role in the design of the study and collection, analysis, interpretation of data, and in writing the manuscript.

Availability of data and materials

Accessing the data is possible with the following procedure. A detailed project must be submitted to the Scientific and Ethics Board of the AP-HP. If the project participants are external to AP-HP, they have to sign a contract with the Clinical Research and Innovation Board (Direction de la Recherche Clinique et de l'Innovation). The project must include the goals of the research, the different steps that will be pursued, a detailed description of the data needed, of the software tools necessary for the processing, and a clear statement of the public health benefits. Once the project is approved, the research team is granted access to the Big Data Platform (BDP), which was created by a sub-department of the IT of the AP-HP. The BDP is a platform internal to the AP-HP where data are collected and that external users can access to perform all their analyses, in accordance with the CNIL regulation. It is strictly forbidden to export any kind of data and each user can access only a workspace that is specific to their project. Each person of the research team can access the BDP

with an AP-HP account after two-factor authentication. If the research team includes people that are not employed by the AP-HP, a temporary account associated to the project is activated.

Declarations

Ethics approval and consent to participate

The AP-HP obtained the authorization of the CNIL (Commission Nationale de l'Informatique et des Libertés, the French regulatory body for data collection and management) in 2017 to share data for research purposes in compliance with the MR-004 reference methodology [73] (authorization N°1980120). The MR-004 reference (<https://www.legifrance.gouv.fr/jorf/id/JORFTEXT000037187498>) controls data processing for the purpose of studying, evaluating and/or researching that does not involve human persons (in the sense of not involving an intervention or a prospective collection of research data in patients that would not be necessary for clinical evaluation, but which allows retrospective use of data previously acquired in patients). The goals of the clinical data warehouse are the development of decision support algorithms, the support of clinical trials and the promotion of multi-center studies. According to French regulation (i.e., the MR-004), and as authorized by the CNIL, patients' consent to use their data in the projects of the CDW can be waived as these data were acquired as part of the clinical routine care of the patients. At the same time, AP-HP committed to keep patients updated about the different research projects of the clinical data warehouse through a portal on the internet (<https://eds.aphp.fr/recherches-en-cours>) and individual information is systematically provided to all the patients admitted to the AP-HP. In addition, a retrospective information campaign was conducted by the AP-HP in 2017: it involved around 500,000 patients who were contacted by e-mail and by postal mail to be informed of the development of the CDW. The project on which the proposed work is based is called APPRIMAGE, it is led by the ARAMIS team (current AP-HP PI: Didier Dormont; initial AP-HP PI: Anne Bertrand, deceased March 2nd 2018) at the Paris Brain Institute and it was approved by the Scientific and Ethics Board of the AP-HP (IRB00011591) in 2018 [77]. All methods were performed in accordance with the relevant guidelines and regulations.

Consent for publication

Not applicable.

Competing interests

The authors declare no competing interests.

Author details

¹Sorbonne Université, Institut du Cerveau - Paris Brain Institute - ICM, CNRS, Inria, Inserm, AP-HP, Hôpital de la Pitié-Salpêtrière, Paris 75013, France. ²Innovation & Données – Département des Services Numériques, AP-HP, Paris 75013, France. ³Hôpital Pitié Salpêtrière, Department of Neuroradiology, AP-HP, Paris 75012, France. ⁴Sorbonne Université, Institut du Cerveau - Paris Brain Institute - ICM, CNRS, Inria, Inserm, AP-HP, Hôpital de la Pitié-Salpêtrière, DMU DIAMENT, Paris 75013, France.

Received: 22 May 2023 Accepted: 7 March 2024

Published online: 20 March 2024

References

1. Heckemann RA, Hammers A, Rueckert D, Aviv RI, Harvey CJ, Hajnal JV. Automatic volumetry on MR brain images can support diagnostic decision making. *BMC Med Imaging*. 2008;8(1):1–6.
2. Morin A, Samper-Gonzalez J, Bertrand A, Ströer S, Dormont D, Mendes A, et al. Accuracy of MRI Classification Algorithms in a Tertiary Memory Center Clinical Routine Cohort. *J Alzheimer Dis*. 2020;74(4):1157–66.
3. Lee JY, Oh SW, Chung MS, Park JE, Moon Y, Jeon HJ, et al. Clinically available software for automatic brain volumetry: comparisons of volume measurements and validation of intermethod reliability. *Korean J Radiol*. 2021;22(3):405.
4. Yu Q, Mai Y, Ruan Y, Luo Y, Zhao L, Fang W, et al. An MRI-based strategy for differentiation of frontotemporal dementia and Alzheimer's disease. *Alzheimer Res Ther*. 2021;13(1):1–12.

5. Zaki LA, Vernooij MW, Smits M, Tolman C, Pama JM, Visser JJ, et al. Comparing two artificial intelligence software packages for normative brain volumetry in memory clinic imaging. *Neuroradiology*. 2022;64:1–8.
6. Koikkalainen J, Rhodius-Meester H, Tolonen A, Barkhof F, Tijms B, Lemstra AW, et al. Differential diagnosis of neurodegenerative diseases using structural MRI data. *NeuroImage Clin*. 2016;11:435–49.
7. Ma D, Lu D, Popuri K, Wang L, Beg MF, Initiative ADN. Differential diagnosis of frontotemporal dementia, alzheimer's disease, and normal aging using a multi-scale multi-type feature generative adversarial deep neural network on structural magnetic resonance images. *Front Neurosci*. 2020;14:853.
8. Penny WD, Friston KJ, Ashburner JT, Kiebel SJ, Nichols TE. *Statistical parametric mapping: the analysis of functional brain images*. Elsevier; 2011.
9. Avants BB, Tustison NJ, Stauffer M, Song G, Wu B, Gee JC. The Insight Toolkit image registration framework. *Front Neuroinformatics*. 2014;8:44.
10. Mark J, Christian FB, Timothy EB, Mark WW, Stephen MS. FSL. *NeuroImage*. 2012;62(2):782–90.
11. Ashburner J, Friston KJ. Unified segmentation. *NeuroImage*. 2005;26(3):839–51.
12. Zhang Y, Brady M, Smith S. Segmentation of brain MR images through a hidden Markov random field model and the expectation-maximization algorithm. *IEEE Trans Med Imaging*. 2001;20(1):45–57.
13. Avants BB, Tustison NJ, Wu J, Cook PA, Gee JC. An open source multivariate framework for n-tissue segmentation with evaluation on public data. *Neuroinformatics*. 2011;9(4):381–400.
14. Wang H, Yushkevich P. Multi-atlas segmentation with joint label fusion and corrective learning—an open source implementation. *Front Neuroinformatics*. 2013;7:27.
15. Ronneberger O, Fischer P, Brox T. U-net: Convolutional networks for biomedical image segmentation. In: *International Conference on Medical image computing and computer-assisted intervention*. Springer; 2015. pp. 234–41.
16. Çiçek Ö, Abdulkadir A, Lienkamp SS, Brox T, Ronneberger O. 3D U-Net: learning dense volumetric segmentation from sparse annotation. In: *International conference on medical image computing and computer-assisted intervention*. Springer; 2016. pp. 424–32.
17. Han X. MR-Based Synthetic CT Generation Using a Deep Convolutional Neural Network Method. *Med Phys*. 2017;44(4):1408–19.
18. Shiri I, Ghafarian P, Geramifar P, Leung KHY, Ghelichoghli M, Oveisi M, et al. Direct attenuation correction of brain PET images using only emission data via a deep convolutional encoder-decoder (Deep-DAC). *Eur Radiol*. 2019;29(12):6867–79.
19. Gong K, Yang J, Kim K, El Fakhri G, Seo Y, Li Q. Attenuation correction for brain PET imaging using deep neural network based on Dixon and ZTE MR images. *Phys Med Biol*. 2018;63(12):125011.
20. Ladefoged CN, Marner L, Hindsholm A, Law I, Højgaard L, Andersen FL. Deep learning based attenuation correction of PET/MRI in pediatric brain tumor patients: evaluation in a clinical setting. *Front Neurosci*. 2019;12:1005.
21. Spuhler KD, Gardus J, Gao Y, DeLorenzo C, Parsey R, Huang C. Synthesis of patient-specific transmission data for PET attenuation correction for PET/MRI neuroimaging using a convolutional neural network. *J Nuclear Med*. 2019;60(4):555–60.
22. Yang J, Park D, Gullberg GT, Seo Y. Joint correction of attenuation and scatter in image space using deep convolutional neural networks for dedicated brain 18F-FDG PET. *Phys Med Biol*. 2019;64(7):075019.
23. Neppi S, Landry G, Kurz C, Hansen DC, Hoyle B, Stöcklein S, et al. Evaluation of proton and photon dose distributions recalculated on 2D and 3D Unet-generated pseudoCTs from T1-weighted MR head scans. *Acta Oncol*. 2019;58(10):1429–34.
24. Wolterink JM, Dinkla AM, Savenije MH, Seevinck PR, van den Berg CA, Išgum I. Deep MR to CT synthesis using unpaired data. In: *International workshop on simulation and synthesis in medical imaging*. Springer; 2017. pp. 14–23.
25. Chen Y, Shi F, Christodoulou AG, Xie Y, Zhou Z, Li D. Efficient and accurate MRI super-resolution using a generative adversarial network and 3D multi-level densely connected network. In: *International Conference on Medical Image Computing and Computer-Assisted Intervention*. Springer; 2018. pp. 91–9.
26. Gu J, Li Z, Wang Y, Yang H, Qiao Z, Yu J. Deep generative adversarial networks for thin-section infant MR image reconstruction. *IEEE Access*. 2019;7:68290–304.
27. Kim KH, Do WJ, Park SH. Improving resolution of MR images with an adversarial network incorporating images with different contrast. *Med Phys*. 2018;45(7):3120–31.
28. Dinkla AM, Wolterink JM, Maspero M, Savenije MH, Verhoeff JJ, Seravalli E, et al. MR-only brain radiation therapy: dosimetric evaluation of synthetic CTs generated by a dilated convolutional neural network. *Int J Radiat Oncol* Biol* Phys*. 2018;102(4):801–12.
29. Emami H, Dong M, Nejad-Davarani SP, Glide-Hurst CK. Generating synthetic CTs from magnetic resonance images using generative adversarial networks. *Med Phys*. 2018;45(8):3627–36.
30. Nie D, Trullo R, Lian J, Wang L, Petitjean C, Ruan S, et al. Medical image synthesis with deep convolutional adversarial networks. *IEEE Trans Biomed Eng*. 2018;65(12):2720–30.
31. Dar SU, Yurt M, Karacan L, Erdem A, Erdem E, Çukur T. Image synthesis in multi-contrast MRI with conditional generative adversarial networks. *IEEE Trans Med Imaging*. 2019;38(10):2375–88.
32. Yu B, Zhou L, Wang L, Shi Y, Fripp J, Bourgeat P. Ea-GANs: edge-aware generative adversarial networks for cross-modality MR image synthesis. *IEEE Trans Med Imaging*. 2019;38(7):1750–62.
33. Li H, Paetzold JC, Sekuboyina A, Kofler F, Zhang J, Kirschke JS, et al. DiamondGAN: unified multi-modal generative adversarial networks for MRI sequences synthesis. In: *International Conference on Medical Image Computing and Computer-Assisted Intervention*. Springer; 2019. pp. 795–803.
34. Sharma A, Hamarneh G. Missing MRI pulse sequence synthesis using multi-modal generative adversarial network. *IEEE Trans Med Imaging*. 2019;39(4):1170–83.
35. Benou A, Veksler R, Friedman A, Raviv TR. Ensemble of expert deep neural networks for spatio-temporal denoising of contrast-enhanced MRI sequences. *Med Image Anal*. 2017;42:145–59.
36. Jiang D, Dou W, Vosters L, Xu X, Sun Y, Tan T. Denoising of 3D magnetic resonance images with multi-channel residual learning of convolutional neural network. *Jpn J Radiol*. 2018;36(9):566–74.
37. Ran M, Hu J, Chen Y, Chen H, Sun H, Zhou J, et al. Denoising of 3D magnetic resonance images using a residual encoder-decoder Wasserstein generative adversarial network. *Med Image Anal*. 2019;55:165–80.
38. Hashimoto F, Ohba H, Ote K, Teramoto A, Tsukada H. Dynamic PET image denoising using deep convolutional neural networks without prior training datasets. *IEEE Access*. 2019;7:96594–603.
39. Du J, Wang L, Liu Y, Zhou Z, He Z, Jia Y. Brain mri super-resolution using 3d dilated convolutional encoder-decoder network. *IEEE Access*. 2020;8:18938–50.
40. Pham CH, Ducournau A, Fablet R, Rousseau F. Brain MRI super-resolution using deep 3D convolutional networks. In: *2017 IEEE ISBI*. IEEE; 2017. pp. 197–200.
41. Zeng K, Zheng H, Cai C, Yang Y, Zhang K, Chen Z. Simultaneous single- and multi-contrast super-resolution for brain MRI images based on a convolutional neural network. *Comput Biol Med*. 2018;99:133–41.
42. Dewey BE, Zhao C, Reinhold JC, Carass A, Fitzgerald KC, Sotirchos ES, et al. DeepHarmony: a deep learning approach to contrast harmonization across scanner changes. *Magn Reson Imaging*. 2019;64:160–70.
43. Xu C, Zhang D, Chong J, Chen B, Li S. Synthesis of gadolinium-enhanced liver tumors on nonenhanced liver MR images using pixel-level graph reinforcement learning. *Med Image Anal*. 2021;69:101976.
44. Seo M, Kim D, Lee K, Hong S, Bae JS, Kim JH, et al. Neural Contrast Enhancement of CT Image. In: *Proceedings of the IEEE/CVF Winter Conference on Applications of Computer Vision*. IEEE; 2021. pp. 3973–82.
45. Bône A, Ammari S, Lamarque JP, Elhaik M, Chouzenoux É, Nicolas F, et al. Contrast-enhanced brain MRI synthesis with deep learning: key input modalities and asymptotic performance. In: *2021 IEEE ISBI*. IEEE; 2021. pp. 1159–63.
46. Kleesiek J, Morshuis JN, Isensee F, Deike-Hofmann K, Paech D, Kicking-ereder P, et al. Can virtual contrast enhancement in brain MRI replace gadolinium?: a feasibility study. *Investig Radiol*. 2019;54(10):653–60.
47. Sun H, Liu X, Feng X, Liu C, Zhu N, Gjermswold-Selleck SJ, et al. Substituting Gadolinium in Brain MRI Using DeepContrast. In: *2020 IEEE ISBI*. IEEE; 2020. pp. 908–12.
48. Bottani S, Thibeau-Sutre E, Maire A, Ströer S, Dormont D, Colliot O, et al. Homogenization of brain MRI from a clinical data warehouse using contrast-enhanced to non-contrast-enhanced image translation with U-Net derived models. In: *SPIE Medical Imaging 2022*. vol. 12032. SPIE; 2022. pp. 576–82.

49. Bottani S, Burgos N, Maire A, Wild A, Ströer S, Dormont D, et al. Automatic quality control of brain T1-weighted magnetic resonance images for a clinical data warehouse. *Med Image Anal.* 2022;75:102219.
50. Gorgolewski KJ, Auer T, Calhoun VD, Craddock RC, Das S, Duff EP, et al. The brain imaging data structure, a format for organizing and describing outputs of neuroimaging experiments. *Sci Data.* 2016;3(1):1–9.
51. Routier A, Burgos N, Díaz M, Bacci M, Bottani S, El-Rifai O, et al. Clinica: An Open-Source Software Platform for Reproducible Clinical Neuroscience Studies. *Front Neuroinformatics.* 2021;15:39. <https://doi.org/10.3389/fninf.2021.689675>.
52. Tustison NJ, Avants BB, Cook PA, Zheng Y, Egan A, Yushkevich PA, et al. N4ITK: improved N3 bias correction. *IEEE Trans Med Imaging.* 2010;29(6):1310–20.
53. Avants BB, Epstein CL, Grossman M, Gee JC. Symmetric diffeomorphic image registration with cross-correlation: evaluating automated labeling of elderly and neurodegenerative brain. *Med Image Anal.* 2008;12(1):26–41.
54. Wen J, Thibeau-Sutre E, Diaz-Melo M, Samper-González J, Routier A, Bottani S, et al. Convolutional Neural Networks for Classification of Alzheimer's Disease: Overview and Reproducible Evaluation. *Med Image Anal.* 2020;63:101694.
55. Milletari F, Navab N, Ahmadi SA. V-net: Fully convolutional neural networks for volumetric medical image segmentation. In: 2016 fourth international conference on 3D vision (3DV). IEEE; 2016. pp. 565–71.
56. Oktay O, Schlemper J, Folgoc LL, Lee M, Heinrich M, Misawa K, et al. Attention U-Net: Learning Where to Look for the Pancreas. In: *Medical Imaging with Deep Learning - MIDL 2018*. 2018.
57. Wang W, Chen C, Ding M, Yu H, Zha S, Li J. Transbts: Multimodal brain tumor segmentation using transformer. In: *International Conference on Medical Image Computing and Computer-Assisted Intervention*. Springer; 2021. pp. 109–19.
58. He K, Zhang X, Ren S, Sun J. Identity mappings in deep residual networks. In: *European conference on computer vision*. Springer; 2016. pp. 630–45.
59. Goodfellow I, Pouget-Abadie J, Mirza M, Xu B, Warde-Farley D, Ozair S, et al. Generative adversarial nets. *Adv Neural Inf Process Syst.* 2014;27.
60. Mirza M, Osindero S. Conditional generative adversarial nets. 2014. arXiv:14111784.
61. Isola P, Zhu JY, Zhou T, Efros AA. Image-to-image translation with conditional adversarial networks. In: *Proceedings of the IEEE conference on computer vision and pattern recognition*. IEEE; 2017. pp. 1125–34.
62. Wei W, Poirion E, Bodini B, Durrleman S, Ayache N, Stankoff B, et al. Predicting PET-derived demyelination from multimodal MRI using sketcher-refiner adversarial training for multiple sclerosis. *Med Image Anal.* 2019;58:101546.
63. Choi H, Lee DS. Generation of structural MR images from amyloid PET: application to MR-less quantification. *J Nucl Med.* 2018;59(7):1111–7.
64. Mao X, Li Q, Xie H, Lau RY, Wang Z, Paul Smolley S. Least squares generative adversarial networks. In: *Proceedings of the IEEE international conference on computer vision*. IEEE; 2017. pp. 2794–802.
65. Morid MA, Borjali A, Del Fiol G. A scoping review of transfer learning research on medical image analysis using ImageNet. *Comput Biol Med.* 2021;128:104115.
66. Mustafa B, Loh A, Freyberg J, MacWilliams P, Wilson M, McKinney SM, et al. Supervised transfer learning at scale for medical imaging. 2021. arXiv preprint arXiv:210105913.
67. Salman H, Ilyas A, Engstrom L, Kapoor A, Madry A. Do adversarially robust imagenet models transfer better? *Adv Neural Inf Process Syst.* 2020;33:3533–45.
68. Wang Z, Bovik AC, Sheikh HR, Simoncelli EP. Image quality assessment: from error visibility to structural similarity. *IEEE Trans Image Process.* 2004;13(4):600–12.
69. Isensee F, Schell M, Pflueger I, Brugnara G, Bonekamp D, Neuberger U, et al. Automated brain extraction of multisequence MRI using artificial neural networks. *Hum Brain Mapp.* 2019;40(17):4952–64.
70. Samper-González J, Burgos N, Bottani S, Fontanella S, Lu P, Marcoux A, et al. Reproducible evaluation of classification methods in Alzheimer's disease: Framework and application to MRI and PET data. *NeuroImage.* 2018;183:504–21.
71. Yi X, Walia E, Babyn P. Generative adversarial network in medical imaging: A review. *Med Image Anal.* 2019;58:101552.
72. Burgos N, Bottani S, Faouzi J, Thibeau-Sutre E, Colliot O. Deep learning for brain disorders: from data processing to disease treatment. *Brief Bioinforma.* 2021;22(2):1560–76.
73. Daniel C, Salamanca E. Hospital Databases. In: Nordlinger B, Villani C, Rus D, editors. *Healthcare and Artificial Intelligence*. Springer; 2020. p. 57–67.
74. Zhao H, Gallo O, Frosio I, Kautz J. Loss functions for image restoration with neural networks. *IEEE Trans Comput Imaging.* 2016;3(1):47–57.
75. Zhu JY, Park T, Isola P, Efros AA. Unpaired image-to-image translation using cycle-consistent adversarial networks. In: *Proceedings of the IEEE international conference on computer vision*. IEEE; 2017. pp. 2223–32.
76. Cackowski S, Barbier EL, Dojat M, Christen T. ImUnity: a generalizable VAE-GAN solution for multicenter MR image harmonization. *Med Image Anal.* 2023;88:102799.
77. Bottani S. Machine learning for neuroimaging using a very large scale clinical datawarehouse [Ph.D. thesis]. Sorbonne Université; 2022.

Publisher's Note

Springer Nature remains neutral with regard to jurisdictional claims in published maps and institutional affiliations.